Force Microscopy with Light-Atom Probes

Stefan Hembacher, Franz J. Giessibl,* Jochen Mannhart

The charge distribution in atoms with closed electron shells is spherically symmetric, whereas atoms with partially filled shells can form covalent bonds with pointed lobes of increased charge density. Covalent bonding in the bulk can also affect surface atoms, leading to four tiny humps spaced by less than 100 picometers in the charge density of adatoms on a (001) tungsten surface. We imaged these charge distributions by means of atomic force microscopy with the use of a light-atom probe (a graphite atom), which directly measured high-order force derivatives of its interaction with a tungsten tip. This process revealed features with a lateral distance of only 77 picometers.

In covalently bound materials, the charge distribution of surface atoms reflects the bonding to the neighbor atoms. Elementary solid state theory predicates that metal bonds are nondirectional and that each metal atom is surrounded by a spherical charge distribution. This simple picture is fairly correct for alkali metals, but it fails for transition metals with partially occupied d shells (*1*–*3*). Pauling (*1*) pointed out that transition metals develop covalent bonding involving hybrid orbitals composed of s, p, and d states. For example, lobes of increased local charge density are present between bulk atoms of a tungsten (W) crystal, as well as on surface atoms. Calculations show that the top layer of a (001) surface of body-centered cubic (bcc) W exhibits a square arrangement of four lobes with increased charge density within a diameter of ≈100 pm (*4*, *5*) (Fig. 1A).

Real-space studies of such charge distributions are in principle possible by scanning tunneling microscopy (STM) (*6*) and atomic force microscopy (AFM) (*7*). However, STM only probes a subset of the electrons surrounding atoms: the most loosely bound electrons with an energy at the Fermi level E_F. Usually, these electrons are less confined in space than the more strongly bonded electrons (*8*). By contrast, AFM can potentially resolve the charge density variations within a single atom because, as Feynman has noted (*9*), the forces in molecules and thus the forces between an AFM tip and sample are the electrostatic forces that all charges distributed over the tip and the sample atoms exert on each other.

The observation of the local charge maxima in W surface atoms requires a microscope with a lateral resolution exceeding 1 Å (100 pm). Is it possible to resolve these extremely localized charge distributions? We used three experimental characteristics to achieve this objective: (i) a light-atom probe, because probe microscopy involves a convolution of a probe atom with the sample atom, and the probe atom should be as small as possible; (ii) a new differential technique with utmost sensitivity to local force variations (*10*); and (iii) a microscope operating at liquid helium temperature, which minimized thermal atomic vibrations and enabled low-bandwidth and correspondingly low-noise measurements.

The basis of the AFM is a cantilever beam with a sharp tip at its end. The force F_{ts} that acts between the tip and the sample maps out an image. Figure 1A represents the front section of an AFM/STM tip near a sample surface. The bottom section shows a W adatom on a W (001) surface. The four red lobes indicate local maxima in the total charge density (*4*, *5*). The charge densities at E_F expose only a single lobe perpendicular to the surface for the W (001) surface (*4*) as well as for a W_5 cluster with similar atomic arrangements (*11*). For both cases, the charge density at E_F does not show the four-leaf-clover symmetry of the total charge density. The white spheres on the top represent C atoms in a graphite surface with a $2p_z$ orbital (pink). Because of the sharp decrease of tunneling probability with increasing distance, the tunneling current is spatially confined to the front atom.

The force between an AFM tip and a sample is a sum of pairwise interaction forces of all tip and sample atoms, and the contribution of the front atom to its next sample atom is often only a small part of the total force. The isolation of the front atom's force contribution from the forces of other atoms requires refined methods [see section III C in (*12*)]. Here, we directly measure higher gradients of F_{ts}. The electrostatic force between two charges at distance r varies as $1/r^2$, and the nth derivative of the electrostatic force with respect to r varies as $1/r^{2+n}$. Hence, the force between two charges reduces to one-fourth when doubling the distance, but the nth derivative of the force with respect to z is $1/2^{2+n}$ times as small. Therefore, higher force derivatives mainly originate from the tip's front atom and the sample atom closest to it. Mapping the crisp spatial variations of higher force derivatives would offer enhanced resolution for AFM. Higher force derivatives couple directly to higher harmonic cantilever oscillations and are conveniently observable with the force-sensing scheme described below.

Most AFMs do not measure the tip-sample force directly. In frequency-modulation AFM (FM-AFM), a cantilever with an eigenfrequency f_0 is driven into an oscillation with a constant amplitude A by supplying positive feedback to an actuator that holds the cantilever. When the cantilever is far from the sample, its deflection is $q'(t) = A\cos(2\pi f_0 t)$. When the distance be-

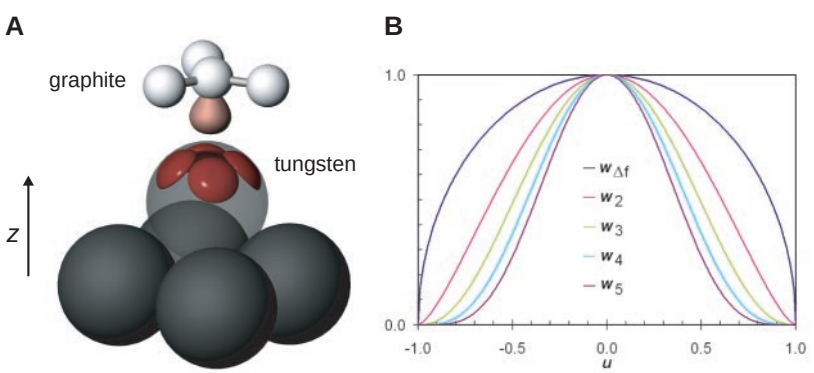

Fig. 1. (**A**) Front section of an idealized tungsten AFM/STM tip with part of a graphite sample on top. The tip consists of bulk W (001) with a bcc crystal structure. In this structure, one atom in the center of a cube is surrounded by eight atoms in the corners of the cube. The front atom of the tip corresponds to an adatom on W (001). The adatom has four local minima in the charge density (*4*, *5*). (**B**) Weight functions $w_{\Delta f}$ and w_2 to w_5 (*13*). The frequency shift is given by a convolution of $w_{\Delta f}$ with the derivative of F_{ts} with respect to z, and the nth harmonic a_n is given by a convolution of w_n with the nth derivative of F_{ts} with respect to z (*13*) (Eq. 1).

Experimentalphysik VI, Elektronische Korrelationen und Magnetismus, Institute of Physics, Augsburg University, 86135 Augsburg, Germany.

*To whom correspondence should be addressed. E-mail: franz.giessibl@physik.uni-augsburg.de

tween cantilever and sample is small enough for F_{ts} to become noticeable, the frequency changes to $f = f_0 + \Delta f$ (*13*). In addition to a shift in frequency, F_{ts} causes harmonic frequency components in the cantilever deflection $q'(t) = \Sigma_{n=0}^{\infty} a_n \cos(n2\pi ft)$. The wealth of information contained in the amplitudes of the higher harmonics a_n was identified in a visionary paper by Dürig (*14*), who proposed to reconstruct F_{ts} for the distance range covered by the oscillating cantilever by analyzing the set of a_n. Here, we focus on an additional useful aspect of higher harmonics: direct coupling to higher derivatives of F_{ts} and thus markedly increased sensitivity to the short-range contributions of F_{ts}. Dürig found that the amplitudes of the nth harmonics a_n can be computed by convoluting F_{ts} in terms of Chebyshev polynomials of order n. It can be shown by integration by parts that a_n can also be expressed as a convolution of the nth derivative of F_{ts} with respect to z with a bell-shaped weight function (*13*):

$$a_n = \frac{2}{\pi k}\frac{1}{1-n^2}\frac{A^n}{1\cdot 3\cdot \ldots \cdot (2n-1)} \int_{-1}^{1} \frac{d^n F_{ts}(z+Au)}{dz^n}(1-u^2)^{n-1/2}du \quad (1)$$

The weight functions $w_{\Delta f}(u) = (1-u^2)^{1/2}$ and $w_n(u) = (1-u^2)^{n-1/2}$ are plotted in Fig. 1B. For amplitudes that are large with respect to the range of F_{ts}, the higher harmonics are essentially proportional to Δf (*15*). When the amplitudes can be reduced to the small values of chemical short-range forces, the higher harmonics a_n are proportional to the higher force gradients that provide enhanced resolution (*13*). In contrast to traditional FM-AFM, the fundamental amplitude $a_1 = A$ in our setup is on the order of the interaction range. Thus, the higher harmonics contain useful information.

We used an ultrahigh vacuum AFM/STM that operates at a base pressure of 10^{-8} Pa and is closely coupled to a liquid He bath at 4.2 K, resulting in an operating temperature of 4.9 K (*16*). Operation in an ultrahigh vacuum is required to obtain clean and atomically well-defined tips and samples, and the operation at low temperature also minimizes the thermal motion of tip and sample atoms (*17*). Constant height operation facilitates the interpretation of simultaneously acquired physical parameters such as tunneling current and higher harmonic amplitudes. Because of the low scanning speed, the signals can be recorded at a small bandwidth and at a correspondingly good signal-to-noise ratio.

The direct approach to measure interatomic charge distributions in tungsten is to probe a W (001) surface. However, the mapping of one atom with another atom involves a convolution of the electronic states of tip and sample atoms. Therefore, the charge distribution of the tip atom should be highly confined to prevent image blurring. Thus, the probing atom needs to be small. This requirement rules out the use of standard tip materials such as silicon, tungsten, or iridium.

Because of its small atomic size, we chose carbon as our probing atom. Highly oriented pyrolytic graphite provides well-defined atomic carbon states, and the layers are extremely stiff in the lateral directions and moderately stiff vertically (*18*). Therefore, the tip and sample switched roles in our experiment, and we used graphite to image a polycrystalline tungsten tip. Graphite has a hexagonal surface lattice with a lattice constant of 246 pm and a basis consisting of two atoms. The α surface atom has a direct neighbor in the graphite layer underneath and is invisible to STM for bias voltages on the order of 100 mV because the electron density at E_F is small at the α site. The electrons at E_F are spatially confined at the β atoms with a $2p_z$ symmetry (*19*). The reciprocity principle of scanning probe microscopy [p. 88 in (*20*)] states that the images are a convolution between the tip and sample atoms and can be viewed equivalently as either an image of N sample atoms probed with one tip atom or N images of one tip atom probed by one out of N sample atoms ($N \approx 6$ in Fig. 2). Thus, probing a surface consisting of small atoms with a tip that has a big front atom corresponds to profiling a bed of N nails with a finger: If one were to analyze the measured profile, one would find N profiles of that same finger.

In the experiment, the graphite sample was freshly cleaved before it was brought into the vacuum. The W tip was sharpened by electrochemical etching (3 V dc) and cleaned in situ by field emission. The tip was mounted on a qPlus force sensor (*21*) to oscillate it and measure the higher harmonics of its periodic deflection. Separate electrodes for tunneling current and deflection signal allowed a simultaneous measurement of the current that flowed between the C and W atoms and the force interactions between them. The sensor had a spring constant of $k = 1.8$ kN/m, an eigenfrequency of $f_0 = 18{,}076.5$ Hz, and a quality factor of $Q = 20{,}000$. The higher harmonics were measured by feeding the cantilever deflection into a programmable eight-pole high-pass filter (Stanford Research Systems SR650) with the lower threshold set to 20 kHz, followed by a root mean square–to-dc converter (*22*).

Three sets of data (Fig. 2, A and B, C and D, and E and F) display parallel measurements of tunneling current (left column) and the amplitudes of the higher harmonics V_{hh} (right column). In all three data sets, the tunneling current reveals approximately spherical images of the W electrons at E_F. The higher harmonics shown in the right

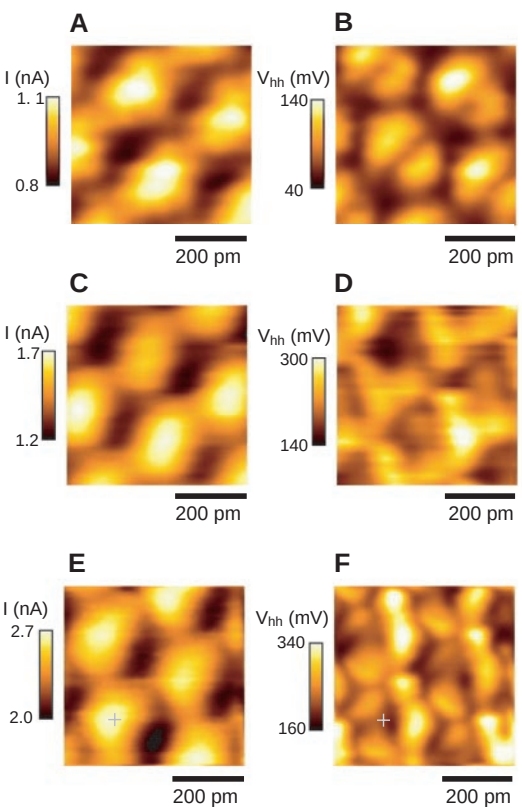

Fig. 2. Constant height measurement of tunneling current I (left column) and amplitudes of higher harmonics V_{hh} (right column). Typical acquisition time is 30 min per data set. The W tip was biased at a voltage of +100 mV with respect to the graphite sample and the fundamental oscillation amplitude was A = 300 pm. (**A**) Tunneling current for a tungsten state showing twofold symmetry in V_{hh} signal. Scanning speed, 1.25 nm/s. (**B**) V_{hh} signal, simultaneously recorded with (A). (**C**) Tunneling current for a tungsten state showing threefold symmetry in the V_{hh} signal. Scanning speed, 200 pm/s. (**D**) V_{hh} signal, simultaneously recorded with (C). (**E**) Tunneling current for a tungsten state showing fourfold symmetry in the V_{hh} signal. Scanning speed, 200 pm/s. (**F**) V_{hh} signal, simultaneously recorded with (E). The V_{hh} signal shows a four-leaf clover, centered close to the maximum of the current image (gray crosses) (Fig. 4). The symmetry of the V_{hh} signals in the right column points to the bonding symmetry of the W tip atom, as shown in Fig. 3.

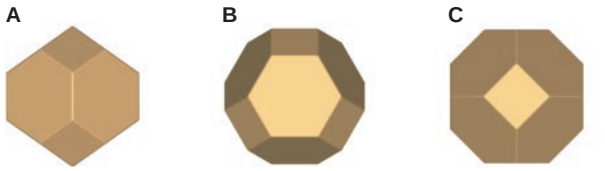

Fig. 3. Wigner-Seitz elementary cell of bcc tungsten. (**A**) View parallel to a ⟨110⟩ crystal direction, showing a twofold symmetry with respect to a rotation around the vertical axis. (**B**) View parallel to a ⟨111⟩ crystal direction with a threefold symmetry. (**C**) View parallel to a ⟨001⟩ crystal direction displaying a fourfold symmetry.

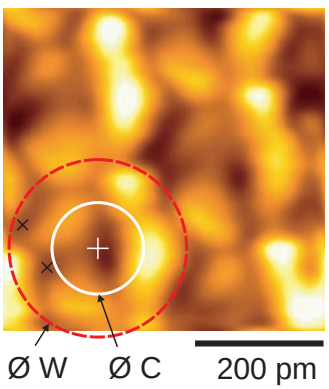

Fig. 4. Magnified view of Fig. 2F, demonstrating a lateral resolution of 77 pm (distance between the black crosses). The solid circle has a diameter of 142 pm, indicating the diameter of a carbon atom. The dashed circle shows the diameter of a tungsten atom (274 pm) (*28*). The white cross marks the center of the circles.

column show much finer details, pointing to a dependence of V_{hh} on the bonding geometry of the W tip atom (*23*). Between the three data sets, tip changes were induced by mild collisions or by field emission until stable imaging occurred again. We thus conclude that for a tungsten tip, several stable configurations are possible in which the W atoms neighboring the front atom occupy high-symmetry positions. Because the electronic structure of an adatom on a W (001) surface reflects its bonding symmetry, we assume that the charge density of adatoms on other high-symmetry surface orientations also reflects the bonding symmetry of the bulk (*24*). The Wigner-Seitz unit cell of a lattice reflects its complete symmetry. Figure 3 shows the Wigner-Seitz cell of bcc tungsten from three angles. Figure 3A is a view parallel to a ⟨110⟩ crystal direction, showing a twofold symmetry, Fig. 3B is a view along a ⟨111⟩ direction with a threefold symmetry, and Fig. 3C is a view from a ⟨001⟩ orientation with a fourfold symmetry. We propose that the W atom was oriented as shown in Fig. 3A in the data of Fig. 2, A and B, oriented as in Fig. 3B in Fig. 2, C and D, and oriented as in Fig. 3C in Fig. 2, E and F.

A first indication of the high-resolution power offered by light-atom probes is apparent in an experiment performed in 1987 by Binnig (*25*), who found in a low-temperature STM experiment that the presence of an STM tip in close vicinity to a graphite sample led to an oscillation of the tunneling current for certain tunneling conditions (tunneling current of 10 nA and a bias voltage of 0.6 V). The oscillation of the current was presumably caused by a flipping of the soft graphite surface layer between two values, and the flip rate was a function of the lateral position of the tip. A map of the flip rate resulted in images showing all carbon atoms spaced by 142 pm and additional structures depending on the flip conditions. The large magnitude of the higher harmonics found in our experiments also points to a periodic flipping of the graphite surface toward the tungsten tip [atomic jump-to-contact process (*26*)], but jump to contact of the complete cantilever can be ruled out because of its stiffness. Flipping is expected to occur when large attractive forces between the tip and the soft graphite layers are present (i.e., when a chemical bond between W and C forms). In AFM measurements of higher harmonics on more rigid samples, such as Si, the magnitude of the higher harmonics is at least one order of magnitude smaller, indicating that flipping is linked to the softness of graphite.

Ohnesorge and Binnig (*27*) have reported sharp spikes marking the onset of attractive interaction in AFM experiments on calcite. Therefore, it could be speculated that the sharp features presented in Fig. 2, B, D, and F, could be caused by several W atoms making contact with the graphite surface. However, such a multitip effect would also be reflected in the simultaneously recorded image of the tunneling current in Fig. 2, A, C, and E. Because the tunneling current image displays only a single peak, we conclude that the structures showing in the higher harmonic signal result from the interaction of two single atoms. The absolute values of tunneling current, frequency shift, and dissipation also point to a single atom contact.

The experimental image with the greatest spatial resolution is Fig. 2F. Figure 4 shows a magnification of this image in which the sizes of C atoms (radius 71 pm) and W atoms (radius 137 pm) (*28*) are indicated by a full and a dashed circle, respectively. The four lobes corresponding to a W atom lie completely within the diameter of one W atom. In agreement with charge density calculations at E_F (*4*, *11*), the peak of the corresponding STM image shown in Fig. 2E is in the center of the four lobes of the higher harmonic images. The distance between the two adjacent local minima marked by black crosses is only 77 pm, demonstrating subangstrom resolution of higher harmonic AFM.

The enhancement in spatial resolution that is possible with light-atom probes and higher harmonic detection appears very attractive for nano- and picoanalytics in physics, chemistry, biology, and materials science. In the future, we expect that the use of tips made of other light-atom materials, such as diamond, beryllium, or hydrogen-terminated materials, will enable exciting revelations on the picometer-length scale.

References and Notes

1. L. C. Pauling, *The Nature of the Chemical Bond* (Cornell Univ. Press, Ithaca, New York, ed. 2, 1948), chap. 11.
2. N. W. Ashcroft, N. D. Mermin, *Solid State Physics* (Holt-Saunders, Philadelphia, PA, 1976).
3. J. Owen, J. H. M. Thornley, *Rep. Prog. Phys.* **29**, 675 (1966).
4. M. Posternak, H. Krakauer, A. J. Freeman, D. D. Koelling, *Phys. Rev. B* **21**, 5601 (1980).
5. L. F. Mattheiss, D. R. Hamann, *Phys. Rev. B* **29**, 5372 (1984).
6. G. Binnig, H. Rohrer, Ch. Gerber, E. Weibel, *Phys. Rev. Lett.* **49**, 57 (1982).
7. G. Binnig, C. F. Quate, Ch. Gerber, *Phys. Rev. Lett.* **56**, 930 (1986).
8. Standard STM operates at typical tip-sample distances of 0.4 to 0.7 nm and maps the charge density at E_F (*20*). The images of single metal atoms are paraboloids with apex radii on the order of 0.5 nm. The exact value depends on tip-sample distance and the electronic states (*20*) with a possible influence of mechanical deformations (*26*). STM operation at smaller tip-sample distances would result in sharper atomic images (*20*, *29*). However, in standard STM, the tip-sample distance must exceed a lower threshold to prevent tip instabilities (*26*), and extremely small tip-sample distances require the use of oscillating STM tips (*30*).
9. R. P. Feynman, *Phys. Rev.* **56**, 340 (1939).
10. After the introduction of the AFM in 1986, the first clear proof of its capability to image single atoms was obtained by imaging the calcite surface in a liquid environment (*27*) in 1993. Reactive surfaces that require imaging in an ultrahigh vacuum, such as the Si (111)-(7×7) surface, were imaged 2 years later (*31*, *32*) with FM-AFM (*33*) with a lateral resolution of ≈0.6 nm. Now, FM-AFM is a routine method (*34*, *12*) for imaging conductive and insulating surfaces with atomic resolution that even enables the direct measurement of chemical-bonding forces (*35*) by using deconvolution techniques (*36*). An optimized sensing technology has led to the observation of subatomic features within a single atom spaced by 220 pm (*37*), related to the orbital structure of a Si atom (*38*). The rest atoms on Si (111)-(7×7) were imaged by low-temperature AFM (*39*) and small-amplitude techniques (*40*), demonstrating a lateral resolution of 384 pm. Repulsive forces vary more strongly with distance than attractive forces and thus offer better spatial resolution (*29*, *41*). FM-AFM probing repulsive interactions can achieve a lateral resolution of 142 pm, demonstrated by resolving the nearest neighbor atoms in graphite (*42*).
11. S. Ohnishi, M. Tsukada, *Solid State Commun.* **71**, 391 (1989).
12. F. J. Giessibl, *Rev. Mod. Phys.* **75**, 949 (2003).
13. The motion of the cantilever is periodic and can be expressed as a Fourier series $q'(t) = \Sigma_{n=0}^{\infty} a_n \cos(n2\pi ft)$. The frequency shift $\Delta f = f - f_0$ is given by $\Delta f = f_0/(\pi k) \int_{-1}^{1} [dF_{ts}(z + Au)/dz] (1 - u^2)^{1/2} du$ (*12*). For $n > 1$, the amplitudes a_n are given by $a_n = 2/(\pi k) f_0^2/(f_0^2 - n^2 f^2) \int_{-1}^{1} F_{ts}(z + a_1 u) T_n(u)\, du/\sqrt{1-u^2}$ (*14*), where $T_n(u)$ denotes the *n*th Chebyshev polynomial of the first kind. Because $f \approx f_0$ and $a_1 = A$, $a_n = 2/(\pi k)\ 1/(1 - n^2)$

$\int_{-1}^{1} F_{ts}(z + Au) T_n(u) du / \sqrt{1-u^2}$. With integration by parts (n times), we find that a_n is given by a weighted average of the nth derivative of F_{ts} (Eq. 1).
14. U. Dürig, *New J. Phys.* **2**, 5.1 (2000).
15. U. Dürig, *Appl. Phys. Lett.* **75**, 433 (1999).
16. S. Hembacher, thesis, Augsburg University, Augsburg, Germany (2003).
17. Because the coefficients of thermal expansion are greatly reduced at temperatures near absolute zero, the thermal drift (i.e., a slow drift of the probe with respect to the sample), a common nuisance in scanning probe experiments, is reduced to 25 pm/hour. The resulting accuracy and time stability permits measurements at very slow scanning speeds and in a constant-height mode, during which the z feedback can be turned off for at least 3 hours while remaining in the tunneling distance regime.
18. We attempted to prepare tips made of doped diamond, but the electrical conductivity of these tips was insufficient for simultaneous AFM/STM operation. Carbon nanotubes might also appear promising as AFM tips, but we require very stiff tips to avoid artifacts from elastic tip deflections.
19. H. Mizes, thesis, Stanford University, Stanford, CA (1987).
20. C. J. Chen, *Introduction to Scanning Tunneling Microscopy* (Oxford Univ. Press, New York, 1993).
21. F. J. Giessibl, *Appl. Phys. Lett.* **76**, 1470 (2000).
22. In our setup, f_0 is small compared with the bandwidth of the deflection detector. Hence, the higher harmonics can be measured with an excellent signal-to-noise ratio. The output voltage of the high-pass filter is given by $V_{hh} = (\sum_2^\infty (S_n a_n)^2)^{1/2}$, where S_n denotes the sensitivity of our deflection sensor for the nth harmonic with $S_n \approx n/(1 + 0.0767n^2)^{1/2} \times 0.1$ mV/pm. S_n is given by the product of the current per deflection generated by the force sensor [equation 2 in (*21*)] times the conversion rate of the preamplifier with $V/I = 10$ megaohms/$(1 + (f/f_{3\,dB})^2)^{1/2}$, where $f_{3\,dB} = 65$ kHz.
23. In addition to the tunneling current and higher harmonic signal, the frequency shift and the dissipation signal were recorded in parallel (*43*). The frequency shift data are similar to the higher harmonic data in the right column of Fig. 2, yet with much less contrast and a substantially smaller signal-to-noise ratio. The resolution of the dissipation data is similar to that of the current data.
24. Notably, the W tip is not an oriented single crystal but the apex of a polycrystalline W wire. The orientation of the tip was not known beforehand in our experiment. However, a tip that provides good STM images exposes a single W atom at the tip apex, and it is reasonable to assume that high-symmetry orientations provide stable tips. The geometry of the next neighbor atoms of the tip could be determined by field ion microscopy (FIM) (*44*), but space constraints prevent the implementation of FIM in our low-temperature AFM/STM.
25. G. K. Binnig, *Phys. Scr.* **T19**, 53 (1987).
26. W. A. Hofer, A. S. Foster, A. L. Shluger, *Rev. Mod. Phys.* **75**, 1287 (2003).
27. F. Ohnesorge, G. Binnig, *Science* **260**, 1451 (1993).
28. The atomic radii of W and C are taken as half the nearest neighbor distance in bulk W [bcc, cubic lattice constant 316 pm (*2*)] and graphite (142 pm), respectively.
29. E. Stoll, *Surf. Sci. Lett.* **143**, L411 (1984).
30. M. Herz, F. J. Giessibl, J. Mannhart, *Phys. Rev. B* **68**, 045301 (2003).
31. F. J. Giessibl, *Science* **267**, 68 (1995).
32. S. Kitamura, M. Iwatsuki, *Jpn. J. Appl. Phys.* **34**, L145 (1995).
33. T. R. Albrecht, P. Grutter, H. K. Horne, D. Rugar, *J. Appl. Phys.* **69**, 668 (1991).
34. R. Garcia, R. Perez, *Surf. Sci. Rep.* **47**, 197 (2002).
35. M. Lantz *et al.*, *Science* **291**, 2580 (2001).
36. U. Dürig, *Appl. Phys. Lett.* **76**, 1203 (2000).
37. F. J. Giessibl, S. Hembacher, H. Bielefeldt, J. Mannhart, *Science* **289**, 422 (2000).
38. M. Huang, M. Cuma, F. Liu, *Phys. Rev. Lett.* **90**, 256101 (2003).
39. M. Lantz *et al.*, *Phys. Rev. Lett.* **84**, 2642 (2000).
40. T. Eguchi, Y. Hasegawa, *Phys. Rev. Lett.* **89**, 266105 (2002).
41. T. R. Albrecht, C. F. Quate, *J. Appl. Phys.* **62**, 2599 (1987).
42. S. Hembacher, F. J. Giessibl, J. Mannhart, C. F. Quate, *Proc. Natl. Acad. Sci. U.S.A.* **100**, 12539 (2003).
43. S. Hembacher, F. J. Giessibl, J. Mannhart, data not shown.
44. H. W. Fink, *IBM J. Res. Develop.* **30**, 460 (1986).
45. We thank G. Binnig, M. Herz, and C. Quate for valuable discussions and comments and C. Quate for encouraging us to perform experiments on graphite. Supported by the Bundesministerium für Bildung und Forschung (project no. 13N6918).

29 April 2004; accepted 25 May 2004
Published online 10 June 2004;
10.1126/science.1099730
Include this information when citing this paper.

Electronic Transitions in Perovskite: Possible Nonconvecting Layers in the Lower Mantle

James Badro,[1]* Jean-Pascal Rueff,[2] György Vankó,[3] Giulio Monaco,[3] Guillaume Fiquet,[1] François Guyot[1]

We measured the spin state of iron in magnesium silicate perovskite $(Mg_{0.9},Fe_{0.1})SiO_3$ at high pressure and found two electronic transitions occurring at 70 gigapascals and at 120 gigapascals, corresponding to partial and full electron pairing in iron, respectively. The proportion of iron in the low spin state thus grows with depth, increasing the transparency of the mantle in the infrared region, with a maximum at pressures consistent with the D″ layer above the core-mantle boundary. The resulting increase in radiative thermal conductivity suggests the existence of nonconvecting layers in the lowermost mantle.

Heat can be transported in the mantle by conduction, radiation, or convection. Convection in the lower mantle is only initiated if the other two processes fail to transfer the heat flux produced from the secular cooling of the core and radioactive decay through the lower mantle, that is, if ratio of heat transport through convection to heat transport through conduction and radiation is high enough. Changes in the conduction or radiation properties of lower-mantle mineral assemblages will therefore strongly affect lower-mantle dynamics (*1–8*).

Earth's lower mantle is mainly composed (*9*) of iron-bearing magnesium silicate perovskite, $(Mg,Fe)SiO_3$, which is the most abundant phase (about 80% by volume), and magnesiowüstite, (Mg,Fe)O. Iron in magnesiowüstite undergoes a high-spin (HS) to low-spin (LS) transition between 60 and 70 GPa (*10*). Such changes can have effects on various properties, such as iron partitioning (*11*) or partial melting (*12*). But, one of the main and intrinsic characteristics of LS iron-bearing minerals resides in the blue shift (*11*, *13*) of iron absorption bands (the absorption bands initially in the infrared (IR) and red region shift to the green-blue region). Here, we show that $(Mg,Fe)SiO_3$, hereafter called perovskite, undergoes two such transitions at lower-mantle pressures. Therefore, both perovskite and magnesiowüstite should become increasingly transparent to red and IR radiation at depths between the bottom third of the mantle and the core-mantle boundary.

We probed the spin state and measured the spin magnetic moment of iron in $(Mg_{0.9},Fe_{0.1})SiO_3$ perovskite from 20 to 145 GPa by using high-resolution Kβ x-ray emission spectroscopy. The measurements were performed on the ID16 inelastic x-ray scattering beam line of the European Synchrotron Radiation Facility (ESRF). The details of the experimental setup (*14*) and sample preparation (*15*) are reported elsewhere. In order to release stresses and to avoid any presence of disordered or amorphous phases, we heated the sample with a neodymium: yttrium-aluminum-garnet (Nd:YAG) laser operating in TEM_{00} (single transverse) mode at each pressure point between 30 and 120 GPa. At higher pressures, laser radiation did not couple with the sample, and heating of the sample was not possible any more.

The spectra (Fig. 1A), which have been vertically shifted for clarity, reveal two transitions associated with a decrease of Kβ′ peak intensity (Fig. 2A) and shifting of the $K\beta_{1,3}$ peak to lower energy (Fig. 2B), occurring around 70 GPa and 120 GPa, respectively. The detailed description of the Kβ process is given elsewhere (*10*). The study of pressure-induced HS-to-LS transitions in geophysically relevant materials (*10*, *16–18*) has recently been possible thanks to the sensitivity of this technique. The emission spectrum

[1]Laboratoire de Minéralogie Cristallographie de Paris (UMR CNRS 7590), Institut de Physique du Globe de Paris, Université Paris, 6 and 7, 4 Place Jussieu, 75252 Paris, France. [2]Laboratoire de Chimie Physique–Matière et Rayonnement (UMR CNRS 7614), Université Paris, 6 11 Rue Pierre et Marie Curie, 75231 Paris, France. [3]European Synchrotron Radiation Facility (ESRF), B.P. 220 F-38043 Grenoble CEDEX, France.

*To whom correspondence should be addressed. E-mail: james.badro@lmcp.jussieu.fr